

New Insights into Structural Evolution of LiNiO₂ Revealed by *Operando* Neutron Diffraction

Po-Hsiu Chien,^[a] Xianyang Wu,^[a,b,c] Bohang Song,^[a] Zhijie Yang^[d], Crystal K. Waters^[d], Michelle S. Everett,^[a] Feng Lin,^[d] Zhijia Du,^{[b],*} and Jue Liu^{[a],*}

[a] Dr. P.-H. Chien, X. Wu, Dr. B. Song, Dr. M. S. Everett, Dr. J. Liu
Neutron Scattering Division
Oak Ridge National Laboratory
Oak Ridge, TN 37830, USA
E-mail: liuj1@ornl.gov

[b] X. Wu, Dr. Z. Du
Electrification and Energy Infrastructures Division
Oak Ridge National Laboratory
Oak Ridge, TN 37830, USA
E-mail: duz1@ornl.gov

[c] X. Wu
School of Mechanical Engineering
Purdue University
West Lafayette, IN 47907, USA

[d] Z. Yang, C. K. Waters, Prof. F. Lin
Department of Chemistry
Virginia Tech
Blacksburg, VA 24061, United States

Supporting information for this article is given via a link at the end of the document.

Abstract: LiNiO₂ (LNO) represents the end member in the compositional space of the LiNi_{1-x-y}Mn_xCo_yO₂ (as x and y approach zero) cathode system. Despite its high theoretical specific capacity (275 mAh/g), LNO suffers from phase transitions with large volume change and unfavorable reactions upon electrochemical cycling, which restricts its practical use in the application of lithium-ion batteries. While the contributing factor to the structural instability commonly linked to the undesired volume collapse associated with the H2–H3 phase transition, detailed analysis of structural evolution following the entire route of phase transitions (H1–M–H2–H3) in real time under battery operating conditions remains a challenging task. In this work, we employ *operando* neutron diffraction to study the structural changes (crystal lattice, Li/Ni–O bond length, O–Ni–O bond angles, and LiO₂/NiO₂ layer thickness) of LNO cathode in a home-built Li_xNiO₂||graphite full cell during Li⁺ de-/intercalation. In particular, the anomalous increase(decrease) of Ni–O(Li–O) bond length at high SOC (> ~85%) in the H3 phase is discussed in the context of O²⁻ → Ni⁴⁺(3d) negative charge transfer.

19 Introduction

The relentless advancement of Li-Ion Batteries (LIBs) technologies stems from the unquenchable demand for higher energy density as the practical application of interest shifts gradually from portable devices to electric vehicles (EVs) large-scale grids.^[3] Since the first report of LiNiO₂ (LNO) in 1954, research efforts have been devoted to assessing the potential of LNO as a cathode material for LIBs.^[5,6] In addition to high theoretical capacity (275 mAh/g), layered LNO, which

is isostructural to LiCoO₂ cathode,^[7] is more economically affordable since nickel has a higher natural abundance than cobalt. However, the hindrance LNO faces prior to commercial use lies in the structural instability,^[8,9] which is fundamentally governed by the degree of Li⁺/Ni²⁺ mixing^[10] and Li⁺/vacancy ordering.^[11] Hence, concerns have been expressed about its electrochemical^[12–14] and thermal^[15,16] performance especially at high degrees of delithiation (> 4.3 V vs. Li/Li⁺). Although extensive works^[17,18] have shown that cation-substituted Ni-rich cathodes, e.g., LiNi_{1-x-y}Mn_xCo_yO₂ (1–x–y ≥ 0.8), can improve the structural/thermal stability and cyclability, the renaissance of research interest in LiNiO₂ has been underway,^[19–23] to meet the harsher criteria for EVs batteries.^[1,2]

Among the challenges such as parasitic surface reactions^[24,25] and formation of disordered rock-salt (NiO) impurity^[26,27] at high state-of-charge (SOC), the sequential phase transition (H1–M–H2–H3)^[28,29] might play a more profound role in altering the structural stability. The reason behind this argument manifests itself when one examines the structural evolution of LNO under cycling. Evidently, a substantial contract of the c-lattice near the end of charge (SOC > ~75%), i.e., due to H2–H3 phase transition,^[28–31] is universally demonstrated to be the leading cause to the structural degradation of LNO. What is worse is the oxygen evolution, despite under active debate over its underlying mechanisms and reversibility,^[24,30,32,33] accompanying the severe lattice distortion. While most studies^[28–30,34–36] employ *in situ/operando* X-ray diffraction to monitor the structural evolution of LNO (or Ni-rich cathodes), little attention is paid to the discussion of local Li/Ni environments, for example, Li/Ni–O bond lengths, as a function of Li content. This can be partially attributed to the relative insensitivity of X-ray to Li. From a structural point of

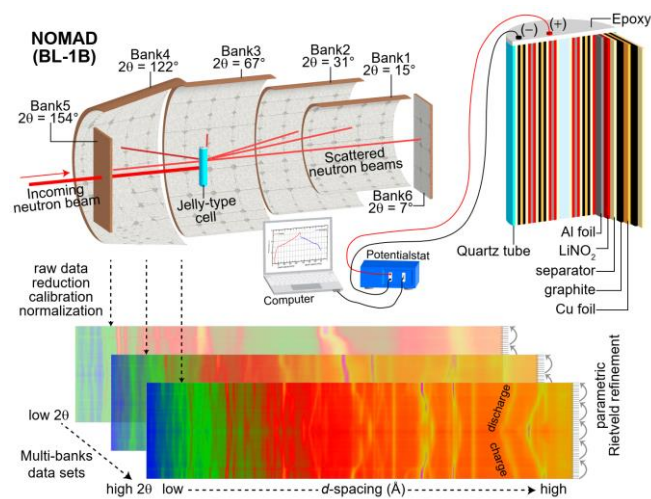
ARTICLE

view, however, it is of central importance to gain a comprehensive understanding beyond how the LNO crystal lattice behaves in response to Li^+ de-/intercalation. It is expected that information, with a focus on the H2–H3 phase transition and single H3 phase region, could be potentially applied to Ni- and/or Co-free cathodes because they are closely related to parent LNO structure.

Compared to X-ray/synchrotron diffraction, neutron diffraction offers several advantages: (1) the neutron scattering length of an element remains constant regardless of momentum transfer (Q). This property enables neutron diffraction to determine the position/occupancy of light elements such as Li with a high level of accuracy, (2) neutron penetrates into the bulk of materials without incurring heating, which prevents unwanted electrochemical reactions when studying the structural evolution of both electrodes in a full cell is desired, and (3) the great contrast in scattering lengths between Li (-2.2 fm), Ni (10.3 fm), and O (5.8 fm) makes neutron diffraction an ideal probe to differentiate their positions in LNO during structural evolution. However, one must be reminded that the neutron flux is weaker than X-ray, not to mention synchrotron. Such intrinsic drawback requires excess loading of active materials (hundreds of milligrams) and longer acquisition time (~ 2 hours or more) to improve the statistics of a neutron powder diffraction (NPD) pattern. Also, the ^1H in organic liquid electrolyte significantly dampens the signal of interest due to a large incoherent scattering length (25.3 fm). As a result, *in situ/operando* neutron diffraction studies^[37–40] are rarely reported with detailed structural information other than crystal lattice of active materials.

with good quality for reliable parametric Rietveld refinements.^[42] Besides, a home-built electrochemical cell makes limited use of the organic liquid electrolyte, thereby minimizing unwanted interference of incoherent scattering from ^1H . In this work, we perform *operando* neutron diffraction study of a model system, i.e., LiNiO_2 ||graphite full cell, on NOMAD with our newly designed cell configuration (Figure 1). We report detailed information on structural evolution of LiNiO_2 cathode (H1–M–H2–H3; H and M denotes hexagonal phase and monoclinic phase, respectively) and graphite anode ($\text{C} \leftrightarrow \text{LiC}_{24} \leftrightarrow \text{LiC}_{12} \leftrightarrow \text{LiC}_6$) in real time at C/10 (cycled between 2.8V and 4.6V). The abnormal change in both the Li/Ni–O bond lengths and $\text{LiO}_2/\text{NiO}_2$ layers thickness across the H2–H3 phase transition ($> \sim 85\%$ SOC) is identified and these anomalies are highly correlated with lattice distortion dictated by the oxygen z-coordinate. Finally, discussion of the unusual increase of the Ni–O bond length in the H3 phase is offered by considering the variation of Ni–O bond covalency as well as the concept of negative charge transfer between O^{2-} (2p) and Ni^{4+} (3d) orbitals.

Results and Discussion

Overview of *operando* neutron diffraction data of LiNiO_2 ||graphite full cell

88

Figure 1. Schematic of *operando* neutron diffraction of LiNiO_2 ||graphite full cell on the NOMAD (BL-1B) beamline at SNS, Oak Ridge National Laboratory. The jelly-type cell with detail cell configuration is shown on the top-right panel. Parametric Rietveld refinements are carried out with TOPAS(v6) on multiple-banks data sets, which are recorded in real time with the event-driven electrochemical cycling.

The high flux neutron powder diffraction/total scattering instrument, Nanoscale Ordered Materials Diffractometer (NOMAD), at the Spallation Neutron Source, Oak Ridge National Laboratory, equips with high neutron flux ($\sim 1 \times 10^8$ neutrons $\text{cm}^{-2} \text{sec}^{-1}$) and large detection coverage (4π steradian).^[41] This allows for rapid acquisition of NPD patterns

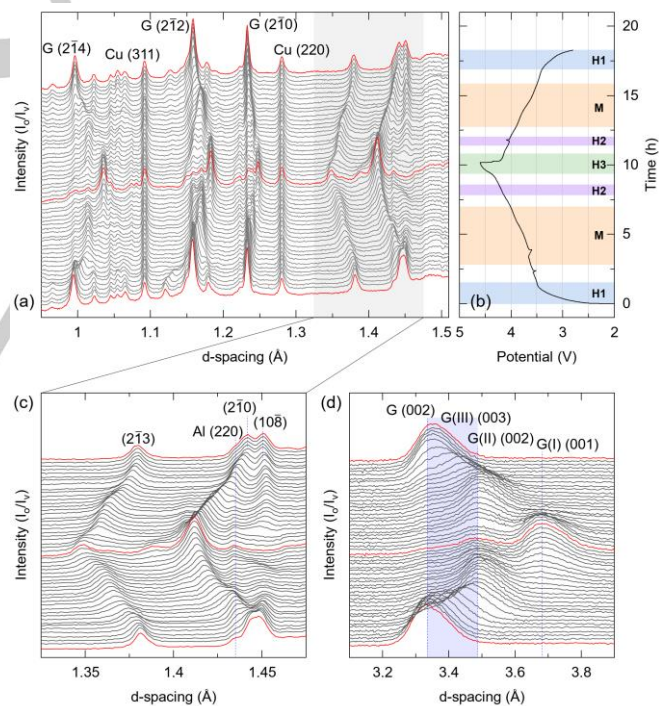


Figure 2. *Operando* neutron diffraction of LiNiO_2 ||graphite full cell for the first cycle. (a) High-resolution bank (Bank 5, $2\theta = 154^\circ$) neutron diffraction patterns. (b) Voltage profile as a function of time. (c) Selected diffraction patterns showing the evolution of Bragg reflections of LiNiO_2 . (d) Selected diffraction patterns (Bank 2, $2\theta = 31^\circ$) showing the evolution of Bragg reflections of lithium-intercalated graphites (G: C_6 , G(III): stage-III (LiC_{24}), G(II): stage-II (LiC_{12}), and G(I): stage-I (LiC_6)).

High-resolution (Bank 5, $2\theta = 154^\circ$) *operando* neutron diffraction patterns of LiNiO_2 ||graphite full cell for the first cycle are shown in

133 **Figure 2a.** The LiNiO_2 ||graphite full cell is cycled at C/10 and the
 134 voltage profile (Figure 2b) is slightly smeared out in the absence
 135 of distinct plateaus^[22] to specify the two-phase (e.g., H2–H3
 136 region^[29,30] (i.e., white areas in between single-phase regions)
 137 Li_xNiO_2 (Determination of cathode composition is described in the
 138 supporting information). Note that the small voltage fluctuation
 139 (drop or spike) is detected as a result of the inevitable vibration of
 140 the bracket which automatically changes the sample holder
 141 during operando operation. Accordingly, the two-phase regions
 142 are mapped out by comparing the evolution of d -spacings of
 143 single phase (see Supporting Information). Overall, the obtained
 144 neutron diffraction patterns permit a clear identification of Bragg
 145 reflections of both cathode and anode components. For example,
 146 while the most intense Bragg reflections with d -spacing < 1.3
 147 can be assigned to Cu current collector ((220) and (311)) and
 148 graphite anode ((2 $\bar{1}$ 0), (2 $\bar{1}$ 2), and (2 $\bar{1}$ 4)), the Bragg reflections of
 149 Li_xNiO_2 cathode ((10 $\bar{8}$), (2 $\bar{1}$ 0), and (2 $\bar{1}$ 3)) are shown in the high
 150 spacing (> 1.3 Å) region (see also Figure 2c).

151 For Li_xNiO_2 , the (2 $\bar{1}$ 0) reflection shifts to lower d -spacing
 152 upon charging, suggesting a continuous contraction of ab plane
 153 during the H1–M–H2–H3 phase transitions. The phenomenon of
 154 two-phase co-existence (e.g., H1–M solid-solution) agrees with
 155 literature results.^[29,30,43] By contrast, the (10 $\bar{8}$) firstly migrates to
 156 higher d -spacing on the verge of the H2 phase region. The
 157 expanded c -lattice then shrinks abruptly once the H2–H3 phase
 158 transition kicks off as reflected by the shift of the (10 $\bar{8}$) reflection
 159 toward a much lower d -spacing (~ 1.38 Å at the end of charge,
 160 see also Figure S1a). Reversible phase transitions, in the context
 161 of unavoidable production of spinel (LiNi_2O_4 or $\text{Li}_{0.5}\text{NiO}_2$)^[15,22,27]
 162 and rock-salt-type (NiO) phases,^[22,23,27] are observed upon
 163 discharging, yet a pronounced splitting of the (10 $\bar{8}$) and (2 $\bar{1}$ 0)
 164 reflections appears after the first cycle (see Figure S1a). This
 165 implies a capacity loss which may relate to (1) the presence of
 166 Ni^{2+} in the Li interslab that minimizes the intercalation of Li^+ ,
 167 and (2) the build-up of solid electrolyte interphase (SEI) on the
 168 graphite anode.

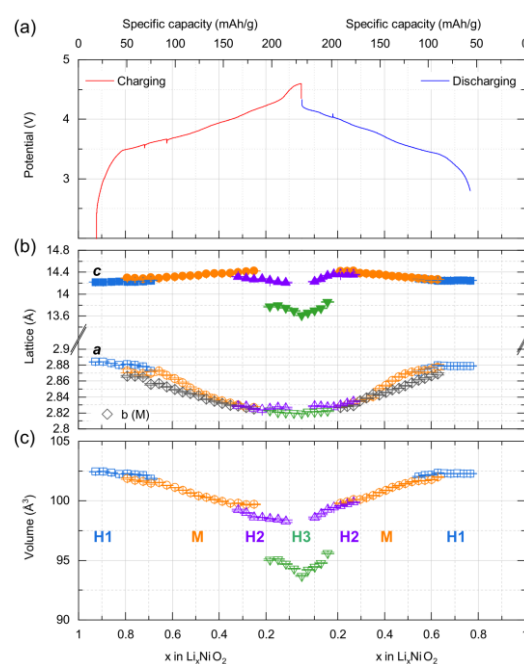
169 In line with literature reports,^[37,45–47] multiple phase
 170 transitions of graphite anode are observed upon electrochemical
 171 cycling (Figure 2d). Upon charging, lithiation of graphite (G)
 172 continuously leads to the development of solid-solution phase
 173 (G(III): LiC_{24}),^[45,47,48] which is then converted to stage-II phase
 174 (G(II): LiC_{12}). Further charging the LiNiO_2 ||graphite full cell
 175 eventually yields the stage-I phase (G(I): LiC_6) at the expense of
 176 the previously formed LiC_{12} via two-phase reaction.^[37] At the end
 177 of charge, a minor fraction of graphite remains unlithiated (see
 178 Figure S1b). The discharge process results in reversible phase
 179 transitions to a large extent, although the (002) reflection of
 180 graphite is not completely matched (i.e., d -spacing and peak
 181 intensity) before/after the first cycle. Therefore, it indicates that a
 182 very small amount of Li^+ , if not negligible, still persists in graphite
 183 anode.

185 Parametric Rietveld Refinements

187 Representative results (SOC = 0%, 50%, 70%, 85%, 100%, and
 188 end of discharge) of parametric Rietveld refinements against the
 189 operando neutron diffraction data of LiNiO_2 ||graphite full cell are
 190 displayed in Figure S2. Reasonable fits of all sets (53 in total) of
 191 diffraction data are obtained (Figure S3) for the first cycle.
 192 Variations in both R_{wp} and G.O.F. (Goodness-Of-Fit) are
 193 inevitably noticed and they can be attributed to the evolution of

two-phase co-existence regions (i.e., transition between two-
 phase region and single-phase region) for both Li_xNiO_2 cathode
 and graphite anode.

Graphite anode. The coupling between the voltage profile
 of LiNiO_2 ||graphite full cell and the graphite phase/lattice
 parameters evolution are shown in Figure S4 and S5. C_6 (G),
 LiC_{24} (G(III): stage-III), LiC_{12} (G(II): stage-II), and LiC_6 (G(I): stage-
 I) are employed to describe the structural evolution of the graphite
 anode. At SOC of 22% ($x = 0.758$ in Li_xNiO_2), LiC_{24} starts to
 develop and reaches its maximal fraction at SOC of 37% ($x =$
 0.623 in Li_xNiO_2), which is then sacrificed for growing LiC_{12} . The
 transition from pristine C_6 to LiC_{24} (stage III) accompanies several
 non-stoichiometric Li_xC_6 phases (e.g., dilute stages)^[47,49,50] with
 specific stacking faults (i.e. faulting probability),^[51] and these
 issues are not incorporated into the parametric Rietveld
 refinements due to the complexity of data analysis and insufficient
 resolution of the current diffraction patterns. In addition, it is
 demonstrated that the formation of the dilute phase LiC_{30} (liquid
 stage II phase) depends heavily on Li^+ kinetics and a slower C-
 rate (at least $< \text{C}/10$; the C-rate used in the present work) is
 required for dilute phases to emerge.^[37,49] Likewise, the
 disappearance of LiC_{24} from neutron diffraction in charging a
 commercial 18650 cell at 1C is also documented.^[52] As a result,
 we avoid to explicitly describe a more sophisticated phase
 transition behavior due to the lack of high temporal resolution of
 our data. $\text{LiC}_{12} \rightarrow \text{LiC}_6$ phase transition occurs at SOC of 55% (x
 $= 0.453$ in Li_xNiO_2) and is not complete at the end of charge,
 in which 14.8% of LiC_6 , 11.7% of LiC_{12} , and 2.7% of unreacted C_6
 are detected. Upon cell discharging (i.e., charging the graphite
 anode), the evolution of phase transitions reverses its sequence
 and lithium-intercalated graphites are recovered at different
 stages. It is worth noting that nearly 100% of Li^+ is
 electrochemically pulled out from both LiC_{12} and LiC_6 (see Figure
 S1b) at the end of discharge. This indicates that the irreversible
 capacity (~ 41 mAh/g; $\sim 18\%$ active Li loss) results primarily from
 the loss of active Li due to the SEI formation in the first cycle. For
 reference, a $\sim 12\%$ capacity loss is typically observed in our jelly-
 type full cells after the first cycle.



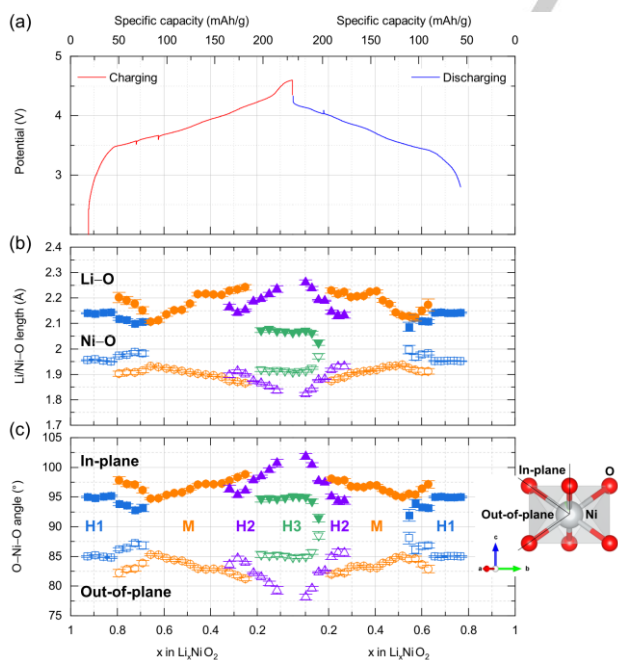
233 **Figure 3.** (a) Voltage profile of LiNiO₂||graphite full cell as a function of Li content
 234 for the first cycle (specific capacity is shown at the top x-axis). (b) Evolution of
 235 lattice parameters (*a* and *c*) of Li_xNiO₂ as a function of Li content derived by
 236 parametric Rietveld refinements. For comparison, the obtained monoclinic
 237 lattice parameters (*a*_M, *c*_M, and *β*) were converted to hexagonal setting (*a*_H and
 238 *c*_H).^[29]

239 **Li_xNiO₂ cathode.** The lattice and volume evolution
 240 Li_xNiO₂ upon de-/intercalation for the first cycle derived from
 241 parametric Rietveld refinements are shown in **Figure 3**. The
 242 refined monoclinic lattice parameters are transformed to
 243 hexagonal setting for comparison.^[29] The onset of phase
 244 transitions (H1–M, M–H2, and H2–H3) in Li_xNiO₂, as compared
 245 literature results^[29,30] using the second cycle for detailed Rietveld
 246 refinements, is slightly “lagged” at higher SOC in the present
 247 work, which deals with the first cycle. The apparent inconsistency
 248 is likely due to (1) the degree of the Li⁺/vacancy ordering
 249 drives the phase transitions^[10,11] and (2) kinetically hindered
 250 phase transition in the first cycle.^[30,36,53] As expected, the *c*-lattice
 251 expands in the H1 and M phases during charging and it
 252 decreases at SOC of ~70% (*x* = 0.318 in Li_xNiO₂) upon the onset
 253 of the M–H2 phase transition. A significant decrease of the
 254 lattice (~85% SOC; *x* = 0.182 in Li_xNiO₂) that initiates the collapse
 255 of the layered structure occurs during the H2–H3 phase transition,
 256 which is a well-known property for Ni-rich cathode materials.
 257^{31,34,35,54]} Indeed, the lattice volume experiences a similar fashion
 258 such that a sudden contraction of the crystal lattice (~3.7% from
 259 H2 to H3) is associated with the growth of the H3 phase during
 260 charging.^[29,30] On the contrary, the *a*-lattice continuously shrinks
 261 upon the removal of Li⁺ from LiO₂ interlayers and it barely
 262 increases near the end of charge. Both the lattice and volume
 263 reversibly attained upon discharging despite ~18% capacity loss

The refined Li/Ni–O bond lengths and O–Ni–O angles (in-
 plane and out-of-plane) as a function of *x* in Li_xNiO₂ upon de-
 /intercalation are summarized in **Figure 4**. The short-range
 structure of LiNiO₂ shows dynamic Jahn-Teller effect, i.e., there
 are four short Ni–O bonds and two long Ni–O bonds. However,
 the average structure of LiNiO₂ can be described using the space
 group (S.G.) *R*–3*m* without long-range Jahn-Teller distortion, and
 this is due to the dynamic nature of the distortion. Therefore, an
 average Ni–O bond lengths [(4 × equatorial Ni–O bond distances
 + 2 × axial Ni–O bond distances)/6] are plotted in Fig. 4b. At first
 glance, the dependency of Li–O and Ni–O bond length on
 electrochemical cycling follows a similar trend as revealed by
 crystal lattice parameters *c* and *a*, respectively. The
 increase(decrease) in Li(Ni)–O bond length echoes with, to a
 certain degree, the evolution of *c*(*a*)-lattice upon charging. When
 Li re-intercalates into the NiO₂ host, reversible behavior is
 reasonably achieved. However, notable features are marked near
 the end of charge (~85% SOC; *x* = 0.182 in Li_xNiO₂). First, the
 Li–O bond length in the H2 phase keeps increasing instead of
 decreasing, as is illustrated in the case of the *c*-lattice as well as
 the lattice volume (Fig. 3b and 3c). Second, the Ni–O bond length
 in the H3 phase elongates abnormally and becomes longer than
 that in the H2 phase, whereas the *a*-lattice of the H2 and H3
 phases is comparably close. The fact that the most evident
 reduction(promotion) of Li(Ni)–O bond length is found in the H3
 phase suggests that the highly delithiated H3 phase is mainly
 responsible for the collapse of layered structure. Consequently,
 this confirms that the improvement of capacity retention of LiNiO₂
 cathode (and Ni-rich cathode materials) can be achieved by
 controlling the upper cutoff voltage^[26,31,34] to intentionally mitigate
 the formation of the H3 phase.

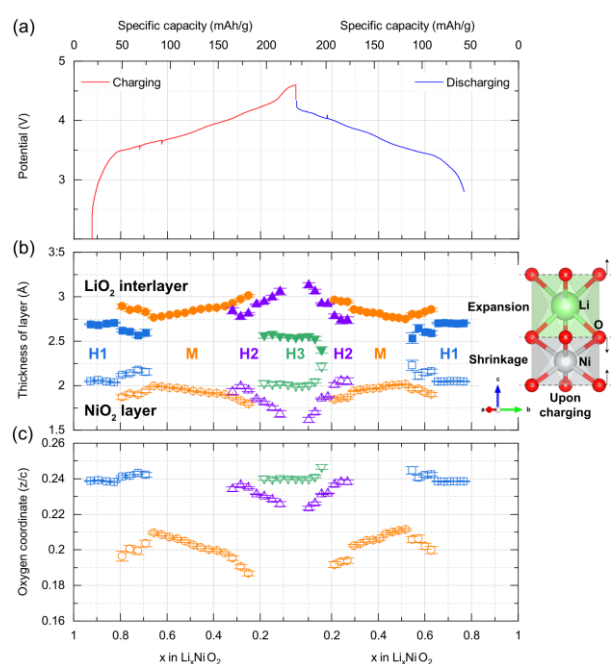
Alternatively, the O–Ni–O angles can be viewed as an
 indicator to examine the local distortion of the NiO₆ octahedra.
 The deviation of the O–Ni–O angles from 90° can be observed
 and opposite developments between the in-plane and out-of-
 plane angles continue to evolve with charging (Fig. 3b). This
 certainly reflects that the NiO₂ slabs are compressed, i.e., highly
 distorted, along with delithiation. In striking contrast, the
 “compression” in the Li⁺-depleted H3 phase (~85% SOC; *x* =
 0.182 in Li_xNiO₂) is released such that its in-plane and out-of-plane
 O–Ni–O angles are almost in line with the level of distortion
 detected in the H1 phase (highly lithiated).

Along the same lines, the thickness of LiO₂ interlayers and
 NiO₂ slabs (**Figure 5**) mirrors the behaviors of the structural
 evolution surveyed by the Li/Ni–O bond lengths and the O–Ni–O
 angles. Indeed, these observations (including *a*- and *c*-lattice) are
 coupled in a sense that they are all governed by the oxygen *z*-
 coordinate (*O_z*) (Figure 5c). In the same way, the change of O–
 O_{interlayer} distance (**Figure 6**) in the NiO₆ octahedra is greatly
 synchronized with the evolution of the NiO₂ slabs thickness. While
 lowering the value of *O_z* during charging typically drives the
 shrinkage of the NiO₂ slabs since the Ni–O bond shortens
 concomitantly, the scenario is conversely played out for the Li–O
 bond in the LiO₆ octahedra, and hence the expansion of the LiO₂
 interlayers. On one hand, the decreasing of the NiO₂ slabs
 thickness (and hence the Ni–O bond length) throughout the phase
 transitions (H1–M–H2) can be understood in the context of
 oxidation of nickel from 3+ (ionic radius: 0.56 Å; low spin) to 4+
 (ionic radius: 0.48 Å).^[55] In addition, Li⁺ de-intercalation causes
 the increase of the Ni–O bond covalency, which reduces the Ni–
 O bond length.^[56,57] On the other hand, it is commonly accepted



264 **Figure 4.** (a) Voltage profile of LiNiO₂||graphite full cell as a function of Li content
 265 for the first cycle (specific capacity is shown at the top x-axis). Evolution of
 266 Li/Ni–O bond length and (c) O–Ni–O bond angles (in-plane and out-of-plane) of
 267 Li_xNiO₂ as a function of Li content derived by parametric Rietveld refinements.
 268

330 that the removal of Li^+ from the LiO_2 interlayers discounts
 331 screening effect of Li^+ on O^{2-} ; therefore, the repulsion
 332 originates from negative charges on oxygen increases, yielding
 333 the observed expansion of the LiO_2 interlayers. In short,
 334 alleviated screening effect by Li^+ and enhanced Ni–O bond
 335 covalency cooperatively exert the influence over the structural
 336 evolution of Li_xNiO_2 upon de-/lithiation, which, in turn, alters
 337 observed change in the LiO_2 (interlayers)/ NiO_2 (slabs) thickness.
 338 However, the anomaly in O_2 upon H2–H3 phase transition at S
 339 of ~85% during charging leads to a decrease, instead of
 340 intuitively expected increase, in the LiO_2 interlayers thickness
 341 (NiO_2 slab shows the opposite trend).



342

343 **Figure 5.** (a) Voltage profile of $\text{LiNiO}_2||\text{graphite}$ full cell as a function of Li content
 344 for the first cycle (specific capacity is shown at the top x-axis). Evolution of (b)
 345 LiO_2 interlayers thickness and (c) NiO_2 slabs thickness as a function of Li content
 346 derived by sequential Rietveld refinements.

347 The abnormal rise of the Ni–O bond length at high levels of
 348 delithiation ($x < \sim 0.2$ in Li_xNiO_2 in the present work) is also
 349 identified in a recent work^[30] (by X-ray diffraction) and our
 350 previous investigations of Ni-rich cathode materials such as
 351 NMC811 or NCA^[58,59]. Conventionally, the average Ni–O bond
 352 lengths are expected to decrease during charging because of
 353 decrease of ionic radii and the increase of the Ni–O covalency.
 354 This agrees well with the observations during the first
 355 transitions (e.g., H1–M and M–H2). Similar finding has been,
 356 for example, demonstrated in LiCoO_2 cathode material and the
 357 decrease of the Co–O bond covalency (upon delithiation) was
 358 experimentally confirmed by O *K*-edge X-ray absorption
 359 spectroscopy^[60] and DFT calculations.^[56] However, the abnormal
 360 increase of the Ni–O bond length in the H3 phase is more likely
 361 triggered by another driving force other than the Ni–O bond
 362 covalency alone.

363 Specifically, we noticed that the negative charge
 364 transfer^[34,56,60,61] has been linked to the anomalous change in the
 365 Ni–O bond length. For example, an abnormal increase of the Ni–
 366 O bond length was captured in $\text{La}_{2-x}\text{Sr}_x\text{NiO}_4$ when x is larger than

1.4.^[62] It is worth mentioning that the nominal oxidation state of
 nickel gradually approaches 4+ with increasing x in $\text{La}_{2-x}\text{Sr}_x\text{NiO}_4$
 and, by analogy, this simulates the situation of local environment
 of Ni^{4+} in the highly delithiated Li_xNiO_2 . Historically, this
 phenomenon can be explained by the negative charge transfer
 between oxygen 2p orbital and nickel 3d orbital that induces
 partial charge transfer from the filled 2p bands in oxygen to the
 strongly p-d hybridized states with predominant Ni 3d parentage.
 The pioneering work by C. N. R. Rao et. al.^[63] has even suggested
 that the oxidation state of nickel in LiNiO_2 should be treated as 2+
 since, via O 1s and Ni 2p_{3/2} X-ray photoelectron spectroscopy,
 they claimed electron holes are created on oxygen by $\text{Ni}^{3+} + \text{O}^{2-}$
 $\leftrightarrow \text{Ni}^{2+} + \text{O}^-$. In other words, an electron hole can be created on
 oxygen by donating an electron from π^* states (2p dominant) to
 σ^* states (strong d-p hybridization). Likewise, $\text{La}_{2-x}\text{Sr}_x\text{CuO}_4$ ^[64]
 also shows significant hole character on oxygen 2p orbitals when
 the concentration of Sr increases. Taken together, charge
 compensation in part leads to the collapse of the *c*-lattice (LiO_2
 interlayers) when the H3 phase emerges because the reduced
 charge concentration on oxygen eventually minimizes the
 coulombic repulsion that initially takes place upon de-intercalation
 of Li^+ from Li_xNiO_2 .

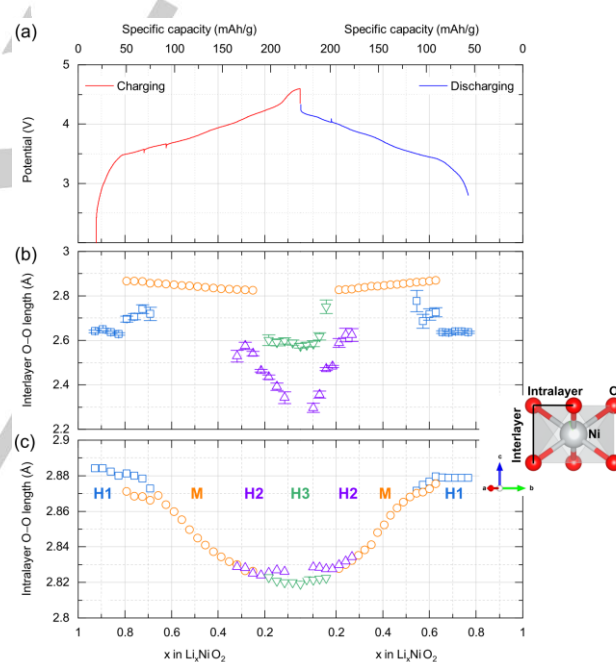


Figure 6. (a) Voltage profile of $\text{LiNiO}_2||\text{graphite}$ full cell as a function of Li content
 for the first cycle (specific capacity is shown at the top x-axis). Evolution of (b)
 interlayer O–O length and (c) intralayer O–O length as a function of Li content
 derived by sequential Rietveld refinements. The evolution of O–O_{interlayer}
 distance basically follows the same trend as illustrated in the *a*-lattice (cf. Fig.
 3).

Of more profound importance to the charge compensation
 is, as suggested by Goodenough et. al.^[62] the $\text{Ni}^{4+} + \text{O}^{2-} \leftrightarrow \text{Ni}^{3+}$
 $+ \text{O}^-$ equilibrium, which hypothetically implies that the Ni–O
 rehybridization upon de-intercalation of Li^+ could keep the
 average oxidation state of nickel to 3+, i.e., the equilibrium tends
 to shift to the right. Indeed, first-principles prediction of Li_xCoO_2
 cathode confirms that the calculated positive charge density on
 cobalt is nearly identical regardless of Li content, e.g., LiCoO_2 ,

Li_{0.5}CoO₂, or CoO₂.^[65] Zunger et. al.^[66] further employs principles quantum mechanical calculations to reveal that “charge self-regulation” generally responds to the change of oxidation state of a transition metal (TM), *cf.*, removing Li⁺ from Li_xNiO₂, and a constant TM charge is recognized. De-lithiation from Li_xNiO₂ (> ~85% SOC in the present work) most likely places the energy level of the empty 3d band (*e_g* dominant) of Ni⁴⁺ lower than that of the 2p band of O²⁻. In this oversimplified scenario, a negative charge transfer ($\Delta CT < 0$) could happen in favor of Ni⁴⁺(3d)-O²⁻(2p) rehybridization. Consequently, the low-lying bonding level substantially features Ni components occupied by electrons, whereas the anti-bonding level is more characterized by oxygen (2p orbital) enriched with holes^[67]. It is also possible that a new intermediate hybridized state, similar to the polaron state, may form between the two major bands through rehybridization at high degrees of delithiation.^[68] These arguments, of course, will need more insights from detailed calculations, specifically tailored for LiNiO₂ cathode system, to verify the complicated electronic structure involving the dynamic change of rehybridization between Ni (3d) and O (2p) atoms under electrochemical cycling. We should also stress that a similar situation (negative charge transfer) has also been reported in other materials including spinel (LiNi_xMn_{2-x}O₄),^[69] nickelate (NdNiO₃),^[70] and a transition-metal halide (Cs₂Au₂Cl₆).^[71] Therefore, it is believed that the structural anomaly, *i.e.*, the collapse of the *c*-lattice near the end of charge, in Ni-rich cathode materials can be broadly attributed to the complex multiple effects as discussed above.

432 Conclusion

433 We carried out the *operando* neutron diffraction on a home-built
434 jelly-type LiNiO₂||graphite full cell charging/discharging at C/10
435 the first cycle. Quantitative analysis is successfully performed
436 using parametric Rietveld refinement to monitor the structural
437 evolution of both Li_xNiO₂ cathode and graphite anode. Detailed
438 information on structural changes including crystal lattice, Li/Ni
439 O bond lengths, LiO₂(interslabs)/NiO₂(slabs) thickness, and
440 Ni–O bond angles are discussed and reported for the first time.
441 In particular, the abnormal variation of the Ni–O bond length in the
442 H3 phase at high SOC (> ~85% in this work) is explained by a
443 simplified scheme (negative charge transfer). It is believed that
444 the commonly observed unusual structural evolution of Ni-rich
445 cathode materials can be justified by the effect of negative charge
446 transfer as well.

447 Experimental Section

448 Experimental details are described in the Supporting Information.

449 Acknowledgements

450 Research conducted at the NOMAD beamlines at ORNL
451 Spallation Neutron Source was sponsored by the Scientific User
452 Facilities Division, Office of Basic Sciences, U.S. Department of
453 Energy. This research at Oak Ridge National Laboratory
454 managed by UT Battelle, LLC, for the U.S. Department of Energy
455 (DOE) under contract DE-AC05-00OR22725, was sponsored by

the Office of Energy Efficiency and Renewable Energy (EERE) Vehicle Technologies Office (VTO). The work at Virginia Tech is supported by the U.S. Department of Energy’s Office of Energy Efficiency and Renewable Energy (EERE) under the award number: DE-EE0008444 (Technology Manager: Peter Faguy).

Conflict of Interest

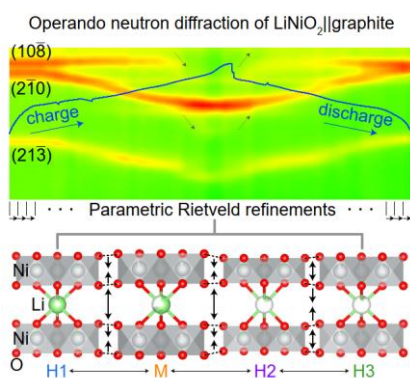
The authors declare no conflict of interest

Keywords: *operando* neutron diffraction • LiNiO₂ • phase transition • structural evolution • lithium-ion batteries

- [1] J. Deng, C. Bae, A. Denlinger, T. Miller, *Joule* **2020**, *4*, 511–515.
- [2] A. Masias, J. Marcicki, W. A. Paxton, *ACS Energy Lett.* **2021**, *6*, 621–630.
- [3] B. Dunn, H. Kamath, J.-M. Tarascon, *Science* **2011**, *334*, 928–935.
- [4] L. D. Dyer, B. S. Borje Jr., G. P. Smith, *Journal of the American Chemical Society* **1954**, *76*, 1499–1503.
- [5] Yu. M. Gulyamov, M. D. Dolgushin, V. P. Morozov, L. N. Sagoyan, *Elektrokhimiya* **1971**, *7*, 896–899.
- [6] A. Yoshino, Y. Masahiko, *Lightweight Secondary Batteries*, **1988**, JP 63121260.
- [7] K. Mizushima, P. C. Jones, P. J. Wiseman, J. B. Goodenough, *Materials Research Bulletin* **1980**, *15*, 783–789.
- [8] J. P. Peres, C. Delmas, P. Biensan, P. Willmann, *J. Phys. Chem. Solids* **1996**, *57*, 1057–1060.
- [9] R. Kanno, H. Kubo, Y. Kawamoto, *Journal of Solid State Chemistry* **1994**, *110*, 216–225.
- [10] C. Poullierie, E. Suard, C. Delmas, *Journal of Solid State Chemistry* **2001**, *158*, 187–197.
- [11] J. P. Peres, F. Weill, C. Delmas, *Solid State Ionics* **1999**, *116*, 19–27.
- [12] T. Ohzuku, A. Ueda, M. Nagayama, *J. Electrochem. Soc.* **1993**, *140*, 1862–1870.
- [13] J. R. Dahn, U. von Sacken, C. A. Michal, *Solid State Ionics* **1990**, *44*, 87–97.
- [14] H. Arai, S. Okada, Y. Sakurai, J.-I. Yamaki, *Solid State Ionics* **1997**, *95*, 275–282.
- [15] H. Arai, S. Okada, Y. Sakurai, J. Yamaki, *Solid State Ionics* **1998**, *109*, 295–302.
- [16] J. R. Dahn, M. Obrovac, *Solid State Ionics* **1994**, *69*, 265–270.
- [17] H.-J. Noh, S. Yoon, C. S. Yoon, Y.-K. Sun, *Journal of Power Sources* **2013**, *233*, 121–130.
- [18] W. Li, E. M. Erickson, A. Manthiram, *Nat Energy* **2020**, *5*, 26–34.
- [19] H. Li, M. Cormier, N. Zhang, J. Inglis, J. Li, J. R. Dahn, *J. Electrochem. Soc.* **2019**, *166*, A429–A439.
- [20] R. Weber, H. Li, W. Chen, C.-Y. Kim, K. Plucknett, J. R. Dahn, *J. Electrochem. Soc.* **2020**, *167*, 100501.
- [21] N. Zhang, J. Stark, H. Li, A. Liu, Y. Li, I. Hamam, J. R. Dahn, *J. Electrochem. Soc.* **2020**, *167*, 080518.
- [22] T. Deng, X. Fan, L. Cao, J. Chen, S. Hou, X. Ji, L. Chen, S. Li, X. Zhou, E. Hu, D. Su, X.-Q. Yang, C. Wang, *Joule* **2019**, *3*, 2550–2564.
- [23] C. Wang, L. Han, R. Zhang, H. Cheng, L. Mu, K. Kisslinger, P. Zou, Y. Ren, P. Cao, F. Lin, H. L. Xin, *Matter* **2021**, S2590238521001193.
- [24] F. Kong, C. Liang, L. Wang, Y. Zheng, S. Peranathan, R. C. Longo, J. P. Ferraris, M. Kim, K. Cho, *Adv. Energy Mater.* **2019**, *9*, 1802586.
- [25] J. Xu, F. Lin, D. Nordlund, E. J. Crumlin, F. Wang, J. Bai, M. M. Doeff, W. Tong, *Chem. Commun.* **2016**, *52*, 4239–4242.
- [26] C. S. Yoon, D.-W. Jun, S.-T. Myung, Y.-K. Sun, *ACS Energy Lett.* **2017**, *2*, 1150–1155.
- [27] S. Ahmed, M. Bianchini, A. Pokle, M. S. Munde, P. Hartmann, T. Brezesinski, A. Beyer, J. Janek, K. Volz, *Adv. Energy Mater.* **2020**, *10*, 2001026.
- [28] W. Li, J. N. Reimers, J. R. Dahn, *Solid State Ionics* **1993**, *67*, 123–130.
- [29] H. Li, N. Zhang, J. Li, J. R. Dahn, *Journal of The Electrochemical Society* **2018**, *10*.
- [30] L. de Biasi, A. Schiele, M. Roca-Ayats, G. Garcia, T. Brezesinski, P. Hartmann, J. Janek, *ChemSusChem* **2019**, *12*, 2240–2250.
- [31] H. Li, A. Liu, N. Zhang, Y. Wang, S. Yin, H. Wu, J. R. Dahn, *Chem. Mater.* **2019**, *31*, 7574–7583.
- [32] J. Cheng, L. Mu, C. Wang, Z. Yang, H. L. Xin, F. Lin, K. A. Persson, *J. Mater. Chem. A* **2020**, *8*, 23293–23303.
- [33] D. Choi, J. Kang, B. Han, *Electrochimica Acta* **2019**, *294*, 166–172.
- [34] A. O. Kondrakov, H. Geßwein, K. Galdina, L. de Biasi, V. Meded, E. O. Filatova, G. Schumacher, W. Wenzel, P. Hartmann, T. Brezesinski, J. Janek, *J. Phys. Chem. C* **2017**, *121*, 24381–24388.

- [35] C. Xu, K. Märker, J. Lee, A. Mahadevegowda, P. J. Reeves, S. J. Day, M. F. Groh, S. P. Emge, C. Ducati, B. Layla Mehdi, C. C. Tang, C. P. Grey, *Nat. Mater.* **2021**, *20*, 84–92.
- [36] A. Grenier, P. J. Reeves, H. Liu, I. D. Seymour, K. Märker, K. M. Wiaderek, P. J. Chupas, C. P. Grey, K. W. Chapman, *J. Am. Chem. Soc.* **2020**, *142*, 7001–7011.
- [37] S. Taminato, M. Yonemura, S. Shiotani, T. Kamiyama, S. Torii, M. Nagao, Y. Ishikawa, K. Mori, T. Fukunaga, Y. Onodera, T. Naka, M. Morishima, Y. Ukyo, D. S. Adipranoto, H. Arai, Y. Uchimoto, Z. Ogumi, K. Suzuki, M. Hirayama, R. Kanno, *Sci Rep* **2016**, *6*, 28843.
- [38] L. Vitoux, M. Reichardt, S. Sallard, P. Novák, D. Sheptyakov, C. Villeveille, *Front. Energy Res.* **2018**, *6*, 76.
- [39] H. Liu, C. R. Fell, K. An, L. Cai, Y. S. Meng, *Journal of Power Sources* **2013**, *240*, 772–778.
- [40] F. Rosciano, M. Holzappel, W. Scheifele, P. Novák, *J Appl Crystallogr* **2008**, *41*, 690–694.
- [41] S. Calder, K. An, R. Boehler, C. R. Dela Cruz, M. D. Frontzek, M. Guthrie, B. Haberl, A. Huq, S. A. J. Kimber, J. Liu, J. J. Molaison, J. Neuefeind, K. Page, A. M. dos Santos, K. M. Taddei, C. Tulk, M. G. Tucker, *Review of Scientific Instruments* **2018**, *89*, 092701.
- [42] G. W. Stinton, J. S. O. Evans, *J Appl Crystallogr* **2007**, *40*, 87–95.
- [43] M. Bianchini, M. Roca-Ayats, P. Hartmann, T. Brezesinski, J. Janek, *Angew. Chem. Int. Ed.* **2019**, *58*, 10434–10458.
- [44] M. G. S. R. Thomas, W. I. F. David, J. B. Goodenough, P. Groves, *Materials Research Bulletin* **1985**, *20*, 1137–1146.
- [45] J. R. Dahn, R. Fong, M. J. Spoon, *Physical Review B* **1990**, *42*, 6424–6432.
- [46] K. P. C. Yao, J. S. Okasinski, K. Kalaga, I. A. Shkrob, D. P. Abraham, *Energy Environ. Sci.* **2019**, *12*, 656–665.
- [47] T. Ohzuku, Y. Iwakoshi, K. Sawai, *J. Electrochem. Soc.* **1993**, *140*, 2490–2498.
- [48] J. R. Dahn, *Phys. Rev. B* **1991**, *44*, 9170–9177.
- [49] C. Didier, W. K. Pang, Z. Guo, S. Schmid, V. K. Peterson, *Chem. Mater.* **2020**, *32*, 2518–2531.
- [50] T. Yao, *Solid State Ionics* **2004**, *175*, 199–202.
- [51] R. E. Johnsen, P. Norby, M. Leoni, *J Appl Crystallogr* **2018**, *51*, 998–1004.
- [52] X.-L. Wang, K. An, L. Cai, Z. Feng, S. E. Nagler, C. Daniel, K. J. Rhodes, A. D. Stoica, H. D. Skorpenske, C. Liang, W. Zhang, J. Kim, Y. Qi, S. J. Harris, *Sci Rep* **2012**, *2*, 747.
- [53] H. Zhou, F. Xin, B. Pei, M. S. Whittingham, *ACS Energy Letters* **2019**, *5*.
- [54] K. Märker, P. J. Reeves, C. Xu, K. J. Griffith, C. P. Grey, *Chem. Mater.* **2019**, *31*, 2545–2554.
- [55] R. D. Shannon, *Acta. Cryst.* **1976**, *A32*, 751–767.
- [56] D.-H. Seo, A. Urban, G. Ceder, *Phys. Rev. B* **2015**, *92*, 115118.
- [57] Y. Koyama, T. Mizoguchi, H. Ikeno, I. Tanaka, *J. Phys. Chem. B* **2005**, *109*, 10749–10755.
- [58] J. Liu, Z. Du, X. Wu, L. Geng, B. Song, P.-H. Chien, M. S. Everette, unpublished results.
- [59] X. Wu, B. Song, P.-H. Chien, M. S. Everette, K. Zhao, J. Liu, Z. Du, unpublished results.
- [60] W.-S. Yoon, K.-B. Kim, M.-G. Kim, M.-K. Lee, H.-J. Shin, J.-M. Lee, J.-S. Lee, C.-H. Yo, *J. Phys. Chem. B* **2002**, *106*, 2526–2532.
- [61] Z. W. Lebens-Higgins, N. V. Faenza, M. D. Radin, H. Liu, S. Sallis, J. Rana, J. Vinckeviciute, P. J. Reeves, M. J. Zuba, F. Badway, N. Pereira, K. W. Chapman, T.-L. Lee, T. Wu, C. P. Grey, B. C. Melot, A. Van Der Ven, G. G. Amatucci, W. Yang, L. F. J. Piper, *Mater. Horiz.* **2019**, *6*, 2112–2123.
- [62] Y. Takeda, R. Kanno, M. Sakano, O. Yamamoto, M. Takano, Y. Bando, H. Akinaga, K. Takita, J. B. Goodenough, *Mat. Res. Bull.* **1990**, *25*, 293–306.
- [63] G. R. Rao, D. D. Sarma, C. N. R. Rao, *Journal of Physics: Condensed Matter* **1989**, *1*, 2147–2150.
- [64] T. Kamiyama, F. Izumi, H. Asano, H. Takagi, S. Uchida, Y. Tokura, E. Takayama-Muromachi, M. Matsuda, K. Yamada, Y. Endoh, Y. Hidaka, *Physica C* **1990**, *172*, 120–126.
- [65] C. Wolverton, A. Zunger, *Phys. Rev. Lett.* **1998**, *81*, 606–609.
- [66] H. Raebiger, S. Lany, A. Zunger, *Nature* **2008**, *453*, 763–766.
- [67] A. E. Bocquet, T. Mizokawa, T. Saitoh, H. Namatame, A. Fujimori, *Phys. Rev. B* **1992**, *46*, 3771.
- [68] Q. Liu, G. M. Dalpian, A. Zunger, *Phys. Rev. Lett.* **2019**, *122*, 106403.
- [69] H. Liu, J. Zhou, L. Zhang, Z. Hu, C. Kuo, J. Li, Y. Wang, L. H. Tjeng, T.-W. Pi, A. Tanaka, L. Song, J.-Q. Wang, S. Zhang, *J. Phys. Chem. C* **2017**, *121*, 16079–16087.
- [70] V. Bisogni, S. Catalano, R. J. Green, M. Gibert, R. Scherwitzl, Y. Huang, V. N. Strocov, P. Zubko, S. Balandeh, J.-M. Triscone, G. Sawatzky, T. Schmitt, *Nat Commun* **2016**, *7*, 13017.
- [71] A. V. Ushakov, S. V. Streltsov, D. I. Khomskii, *J. Phys.: Condens. Matter* **2011**, *23*, 445601.

Entry for the Table of Contents



Operando neutron diffraction was employed to track the phase transitions of LiNiO_2 cathode and graphite anode during charging/discharging at C/10 for the first cycle in real time. Anomalous Li/Ni–O bond lengths in the H3 phase (LiNiO_2) were identified and rationalized by the effect of negative charge transfer through $\text{Ni}^{4+}(3d)\text{--O}^{2-}(2p)$ rehybridization.